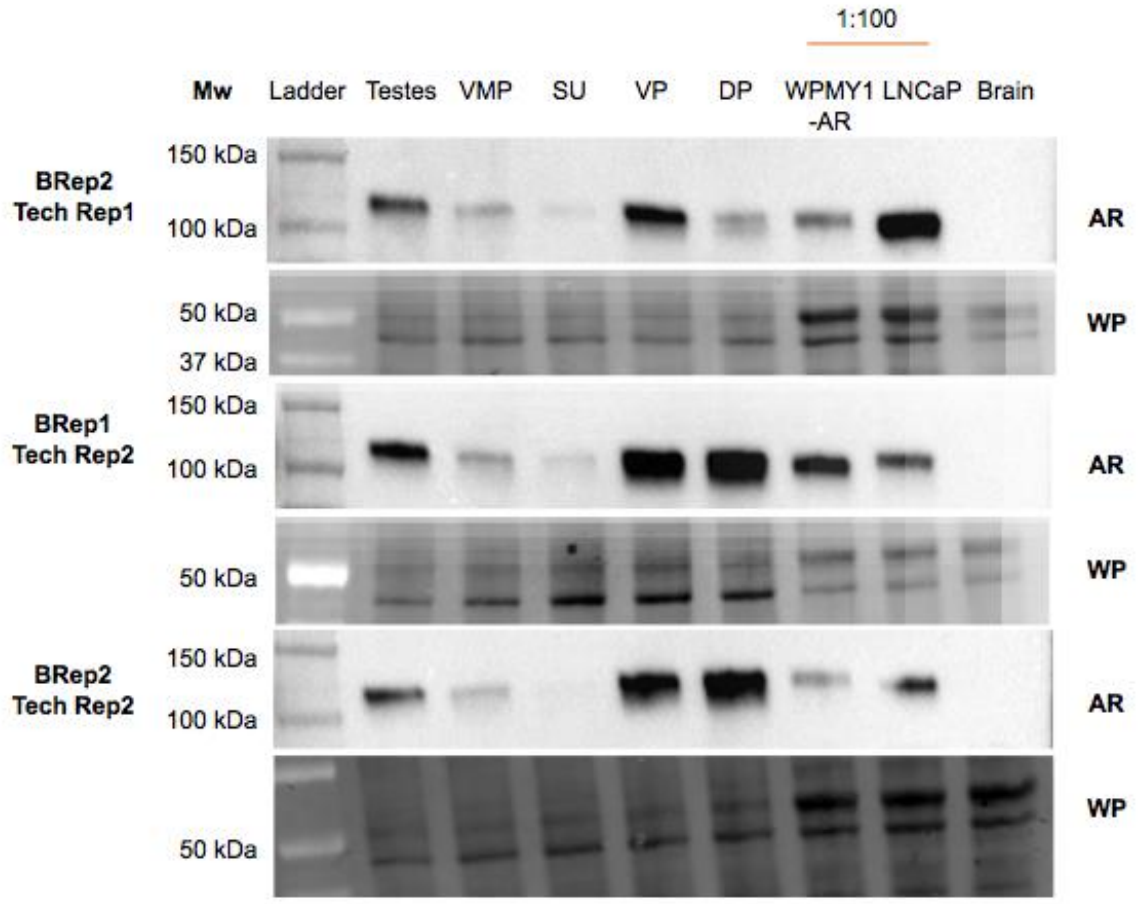

Figure S1 AR protein expression of P0 rat tissues. Western blot analysis of AR (110kDa) and whole protein stain-free blot (WP); mixed male and female P0 rat brain tissue (negative control), male P0 testes, human WPMY1-AR and LNCaP cell lines diluted 1:100 in brain tissue protein (positive controls), female VMP and SU P0 rat and male VP and DP P0 rat tissues. Blotting was repeated 4 times (2 biological replicates and 2 technical replicates of each biological replicate) with 3 replicate runs represented here.

Disease Models & Mechanisms • Supplementary information

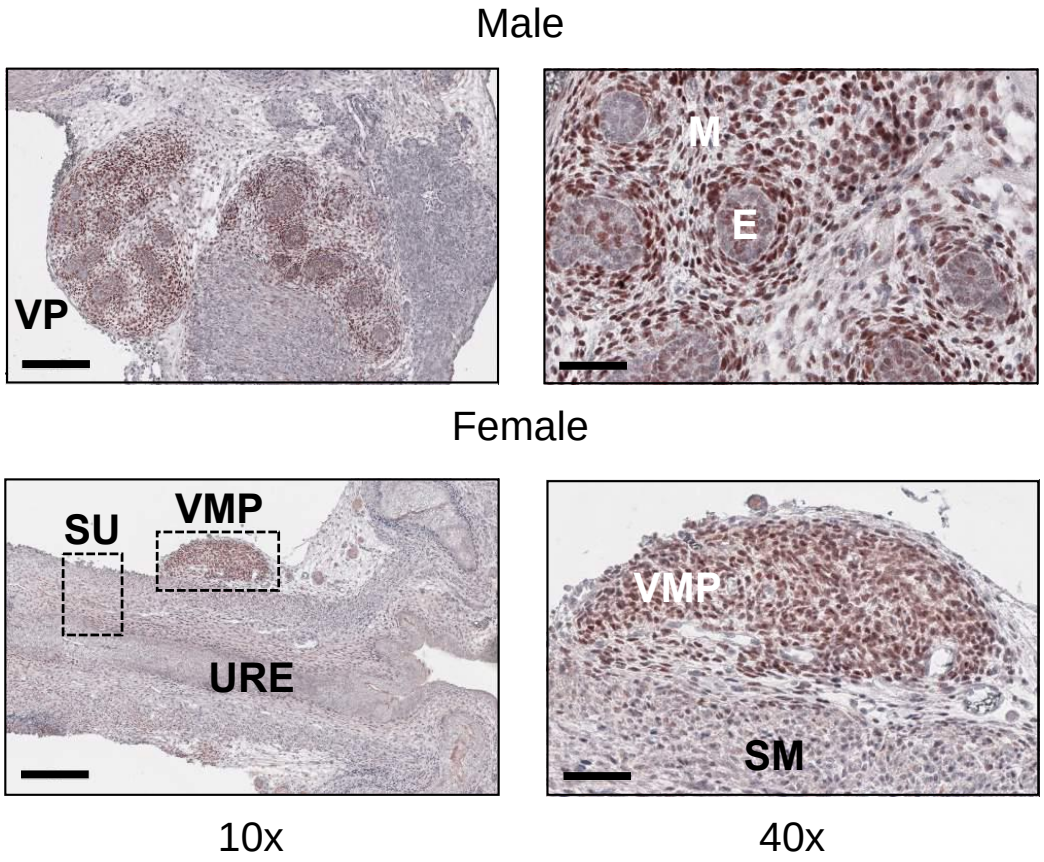

Figure S2 Validation of mesenchymal enrichment of AR in P0 rat tissues. Immunohistochemistry of AR in female UGT (VMP and SU) and male ventral prostate (VP). AR was largely restricted to mesenchymal cells (M) with little AR expression in epithelium (E) of the VP. AR was enriched in VMP cells of the female UGT versus smooth muscle (SM). Scale bars 10x = 200μm, scale bars 40x = 50μm.

Disease Models & Mechanisms • Supplementary information

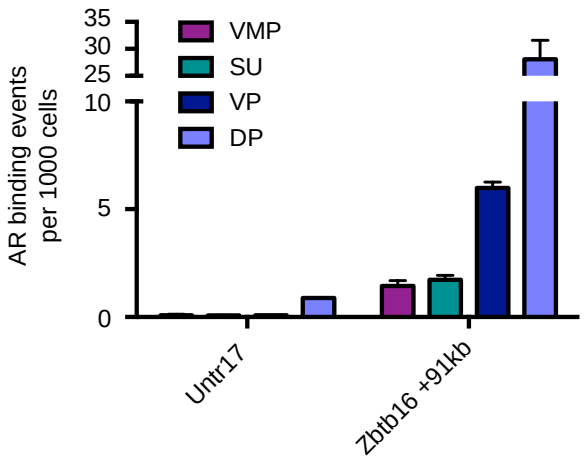

	Enr vs Input
VMP	1.44
SU	1.73
VP	5.99
DP	28.07

Figure S3 AR ChIP-qPCR of control genomic region of P0 rat tissues. Enrichment of AR binding in VMP, SU, VP and DP tissues at a positive control genomic location +91kb downstream from the Zbtb16 gene is expressed as number of AR binding events per 1000 cells normalized against input controls. The histogram illustrates the highest AR enrichment in male tissues. Negative control region represents an untranslated region present on chromosome 17. Bars denote mean from three technical replicate qPCR wells and error bars standard deviation of the mean (SD).

Disease Models & Mechanisms • Supplementary information

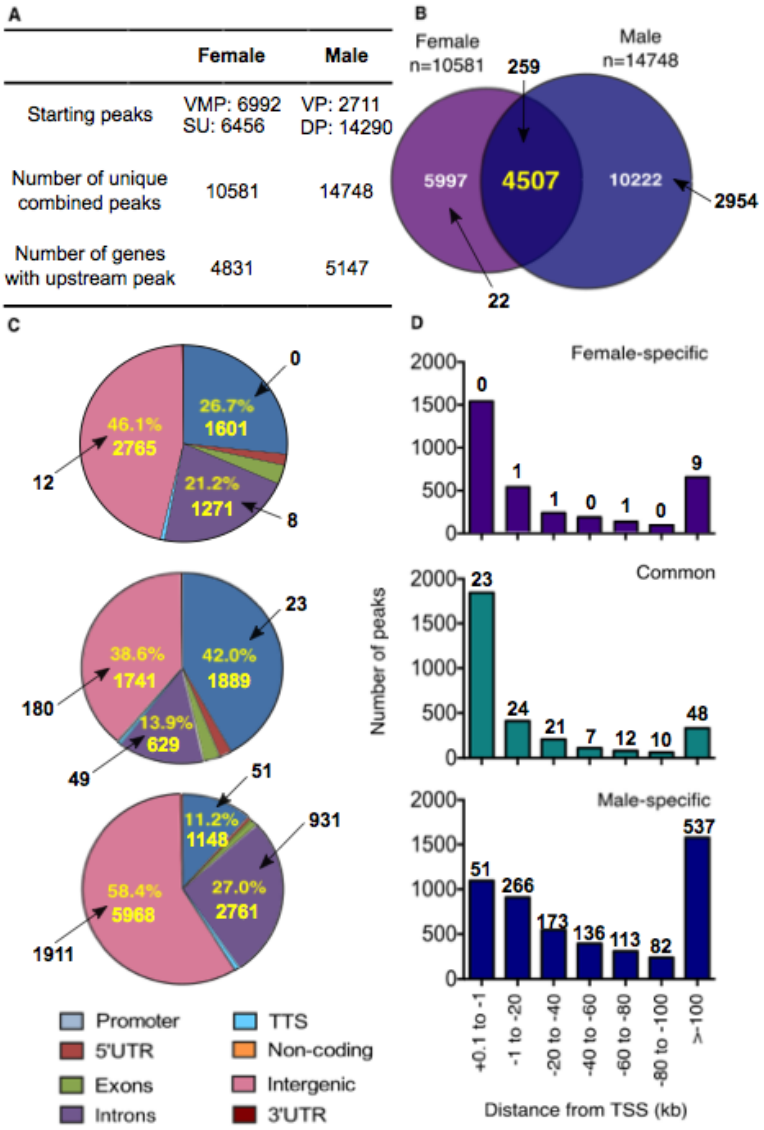

Figure S4 Identification and characterization of sexually dimorphic AR peaks. **(A)** An overview of female and male AR ChIP-seq peak datasets. Table includes the numbers of peaks combined to form the female AR peak set from VMP and SU and male AR peak set from VP and DP and the number of genes associated with a peak upstream from the transcriptional start site (TSS). **(B)** Venn diagram illustrating the overlap of female and male AR peaks. 4507 peaks are co-identified in females and males. 5997 were identified as specific to female and 10222 were specific to male. Arrows depict the number of peaks that contain a classical Androgen Responsive Element (ARE). **(C)** Genomic location analysis of sexually dimorphic and common AR peaks in comparison to the whole genome (Rnor 6.0). Numbers in yellow correspond to proportions of peaks in the genomic region. Arrows depict the number of peaks in the region that contain a classical ARE. **(D)** Genomic location analysis of female-specific, common and male-specific AR peaks upstream of gene TSS respectively. Numbers in bold correspond to the number of peaks in the region that contain a classical ARE.

Disease Models & Mechanisms • Supplementary information

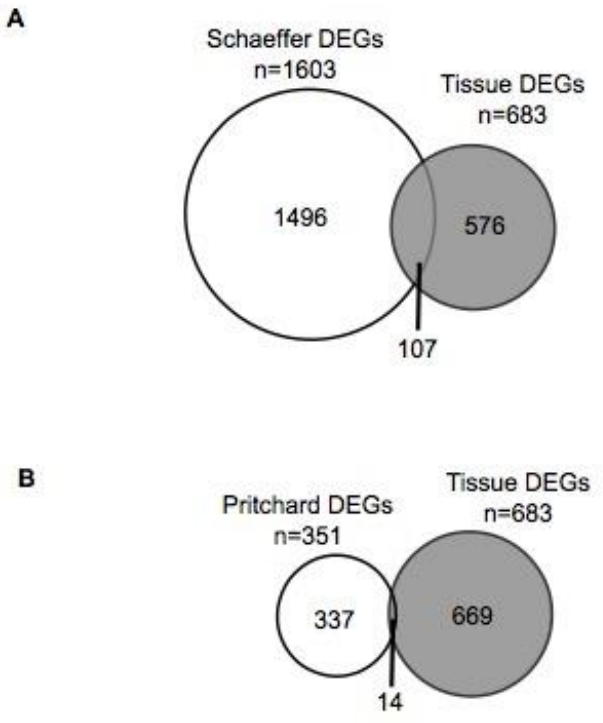

Figure S5 Comparison of sexually dimorphic VMP and VP genes from tissue RNA-seq with murine androgen-responsive and prostate developmental tissue targets. **(A)** Venn diagrams illustrating the overlap of sexually dimorphic VMP and VP genes derived from whole tissue RNAseq (Tissue DEGs) with androgen-responsive genes from the developing murine urogenital sinus (Schaeffer DEGs) (Schaeffer et al., 2008). **(B)** Venn diagrams illustrating the overlap of sexually dimorphic VMP and VP genes derived from whole tissue RNAseq with markers of murine prostate organogenesis (Pritchard DEGs) (Pritchard et al., 2009).

Disease Models & Mechanisms • Supplementary information

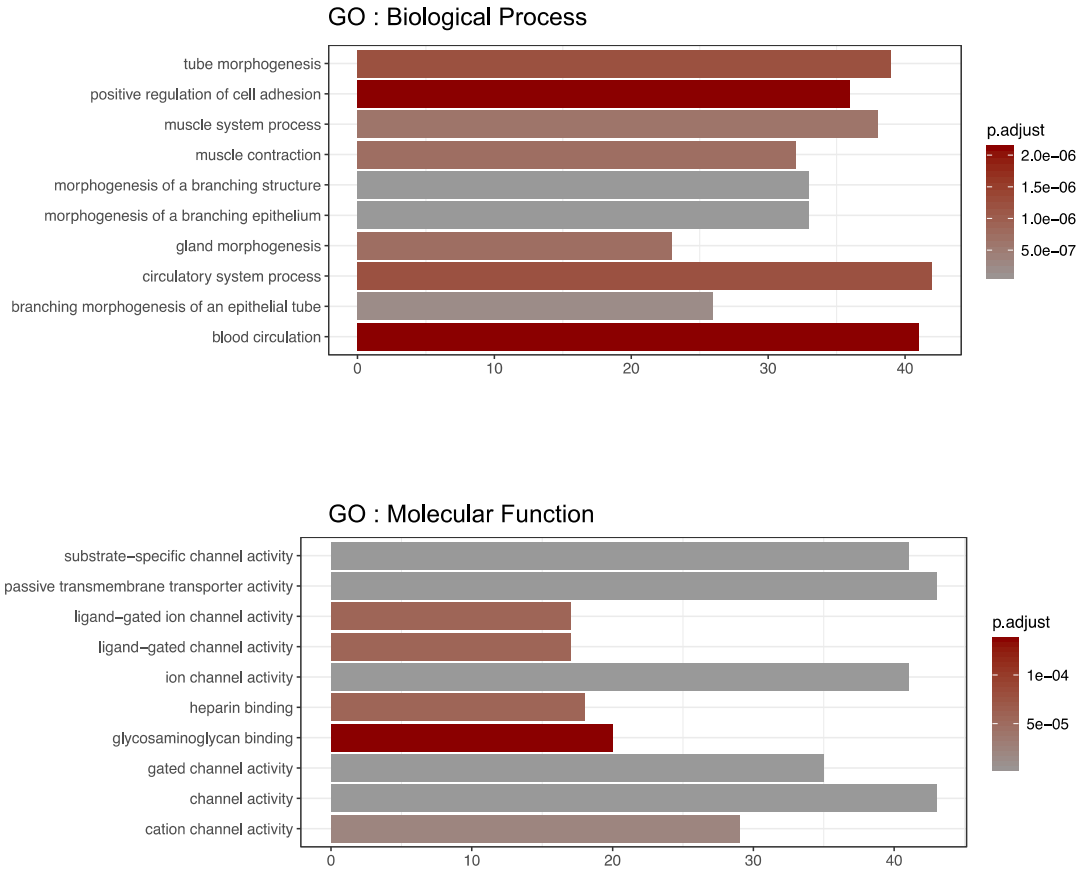

Figure S6 Gene ontology analysis of sexually dimorphic genes derived from whole tissue RNA-seq. The figures represent biological process groups and molecular function groups found with an FDR adjusted P-value >0.05 (p-adj.). Bar lengths represent the number of genes in each group and the shade of colour the p-adj for enrichment.

Disease Models & Mechanisms • Supplementary information

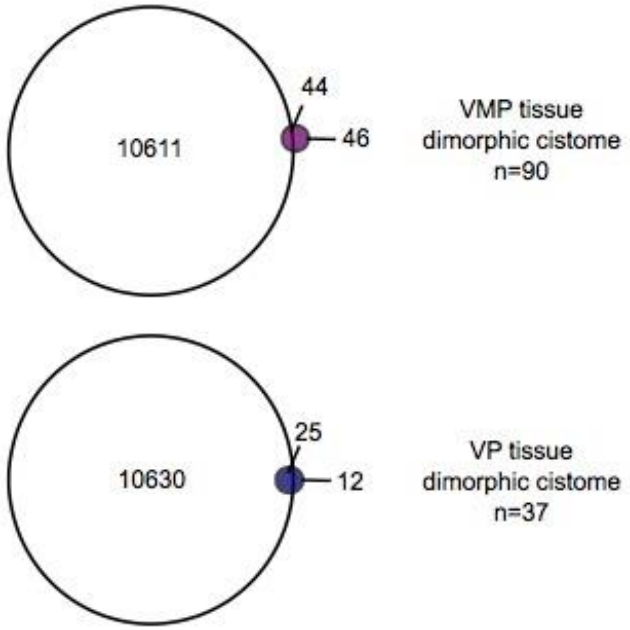

Figure S7 Identification of tissue RNA-seq sexually dimorphic VMP and VP AR target genes with human foetal prostate tissue. Venn diagrams illustrating the overlap of sexually dimorphic VMP and VP AR target genes derived from whole tissue RNAseq with the human foetal prostate transcriptome (Human EMB) (Nash et al., 2018, Orr et al., 2012).

Disease Models & Mechanisms • Supplementary information

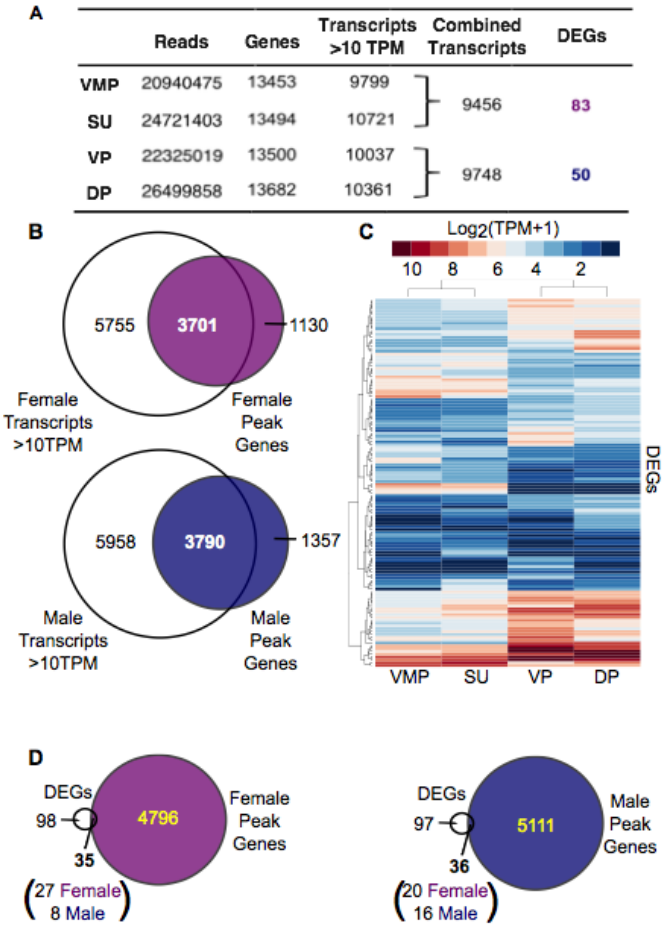

Figure S8 Identification of female and male whole tissue cistromes. **(A)** An overview of RNA-seq transcriptomes of female (VMP & SU) and male (VP & DP) detailing the number of paired reads mapped to the rn6 genome, the number of mapped genes, number of transcripts with read counts > 10 transcripts per million (TPM), the number of combined genes for female and male and the number of differentially expressed genes between female and male identified by NOISeq (DEGs, female enriched in purple and male enriched blue). **(B)** Female and male peaks datasets were generated by combining VMP and SU peaks (female) and VP and DP peaks (male) using HOMER mergePeaks. Genes associated with upstream AR peaks (between +100 and -100,000bp upstream of the transcription start site) from female and male (4831 Female Peak Genes and 5147 Male Peak Genes) were transcript validated with RNAseq data. Venn diagrams illustrate 3701 (77%) and 3790 (74%) genes with an upstream AR peak have read counts > 10 TPM in female and male transcriptomes respectively. **(C)** Heatmap representing the $\log_2$ expression values (TPM+1) of the 133 DEGs identified by NOISeq between female and male tissues. **(D)** Venn diagrams illustrating 35 DEGs (27 female enriched and 8 male enriched) overlap with genes associated with an upstream AR peak in female and 36 DEGs (20 female enriched and 16 male enriched) overlap with genes with an upstream AR peak in males.

Disease Models & Mechanisms • Supplementary information

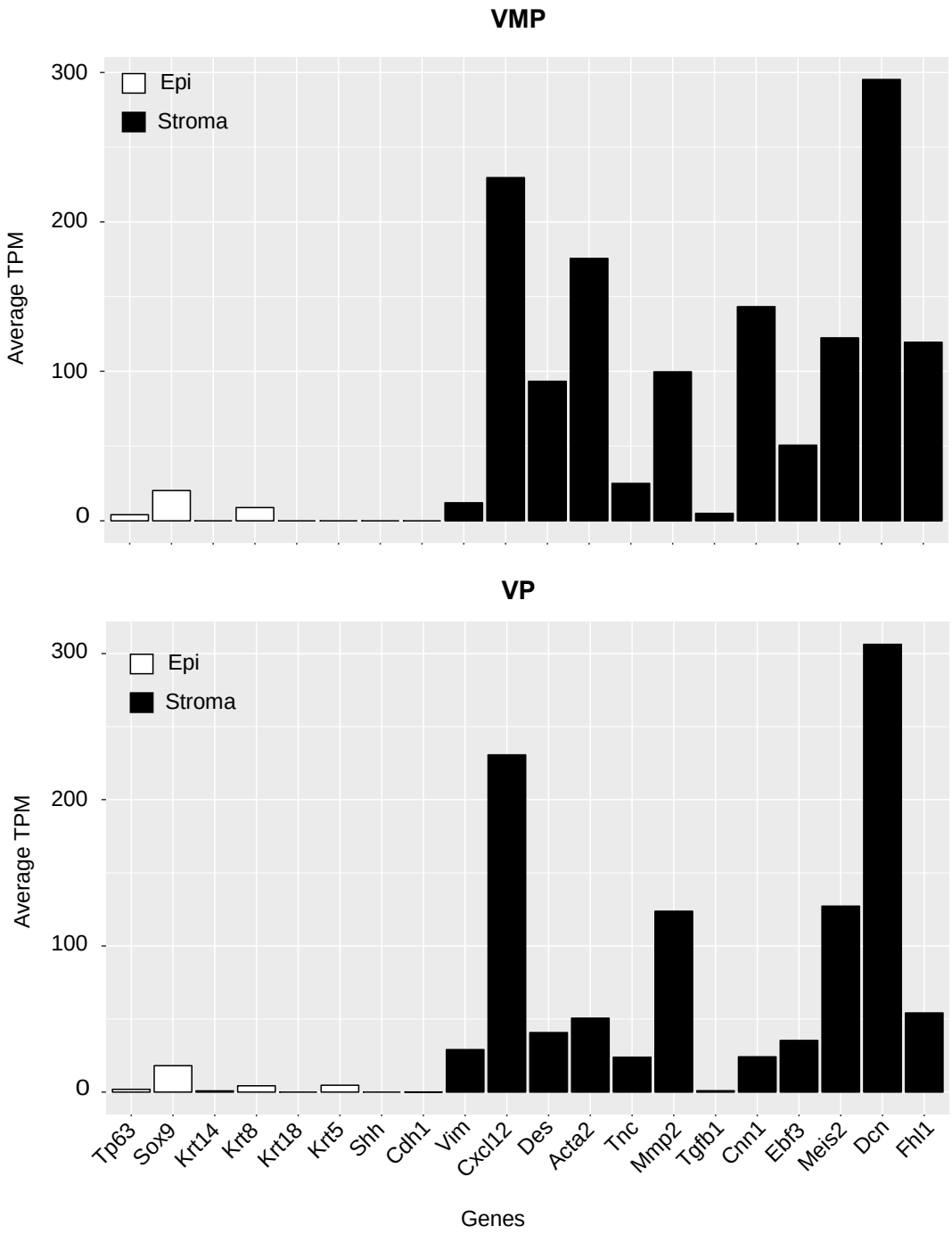

Figure S9 Expression of epithelial and stromal markers in single cell RNA-sequencing data. Bar graphs detailing the average expression in transcripts per million (TPM) of a panel on known epithelial markers (white bars) and stromal markers (black bars) across all VMP cells (top) and VP cells (bottom). Graphs show an enrichment of stromal markers versus epithelial markers in both single cell datasets.

Disease Models & Mechanisms • Supplementary information

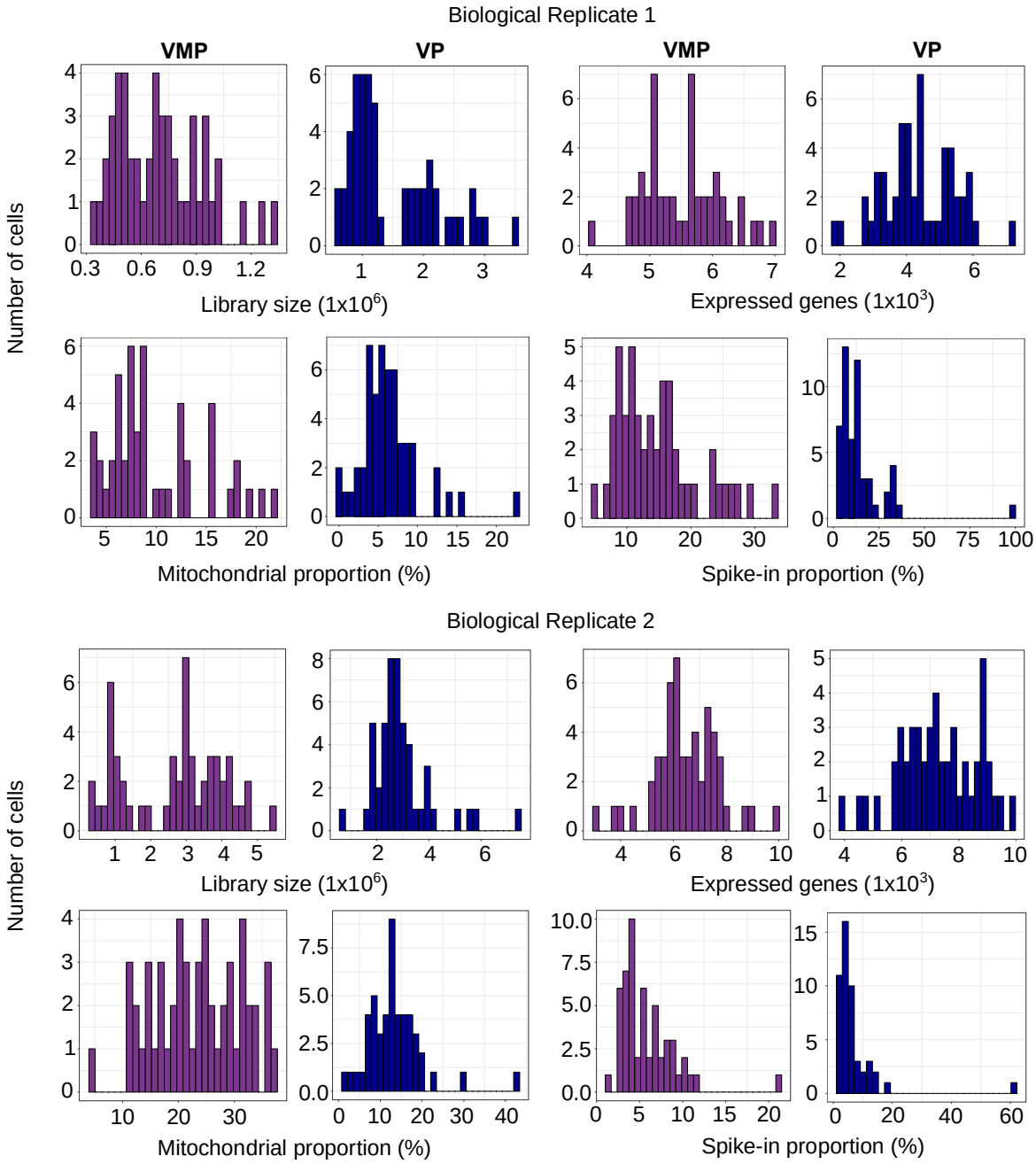

Figure S10 Quality control of VMP and VP single cell RNA-sequencing data. Histograms show the number of cells against library size (per million), number of reads mapped to genes (per thousand), percentage of reads mapping to mitochondrial DNA and percentage of reads mapping to spike-in control DNA. Results from 2 separate biological replicate experiments are shown.

Disease Models & Mechanisms • Supplementary information

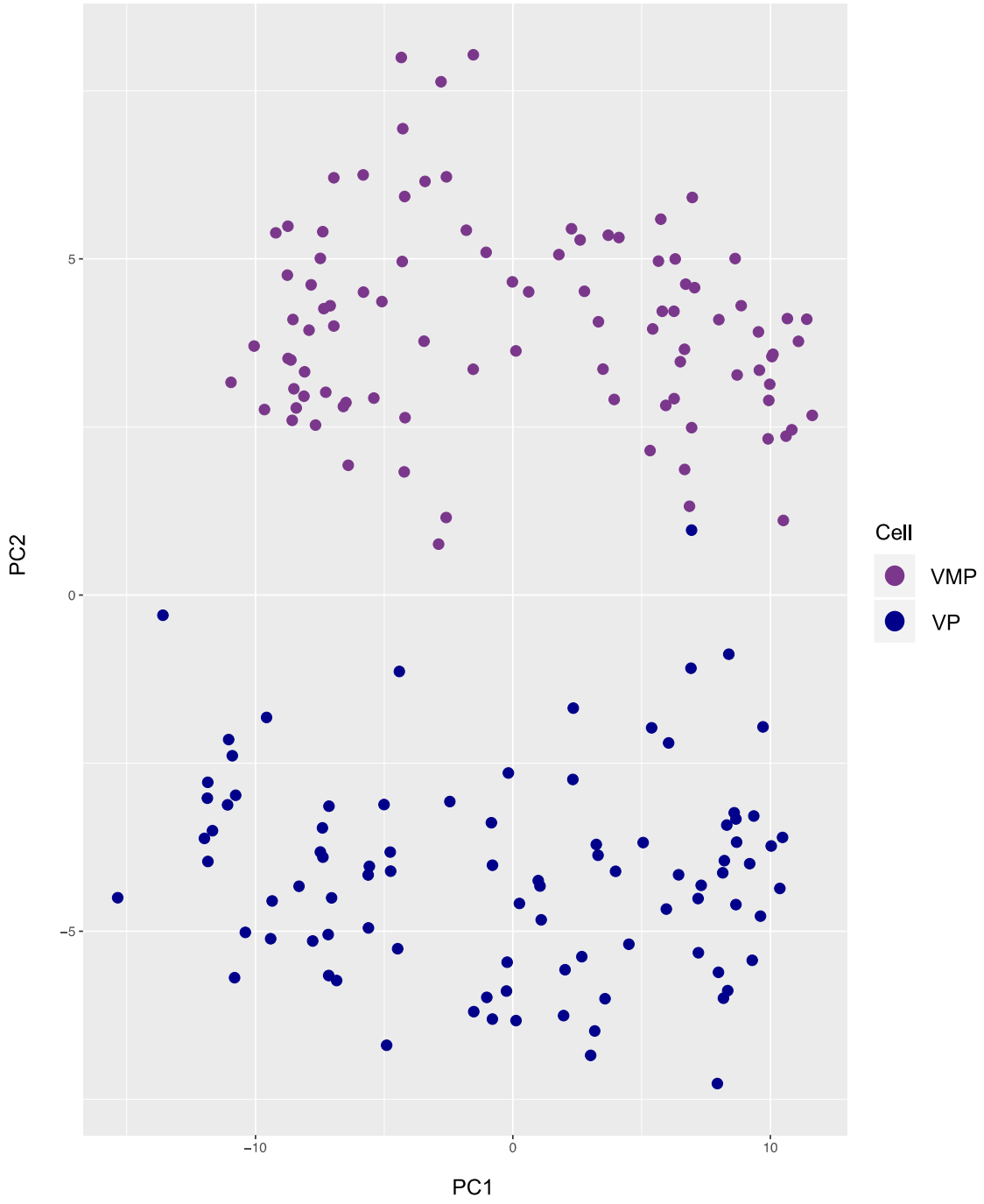

Figure S11 Principal components analysis of combined VMP and VP cell dataset. PCA visualization of VMP (purple) and VP (blue) cells in 2D space shows clear separation of cells into their original tissue types.

Disease Models & Mechanisms • Supplementary information

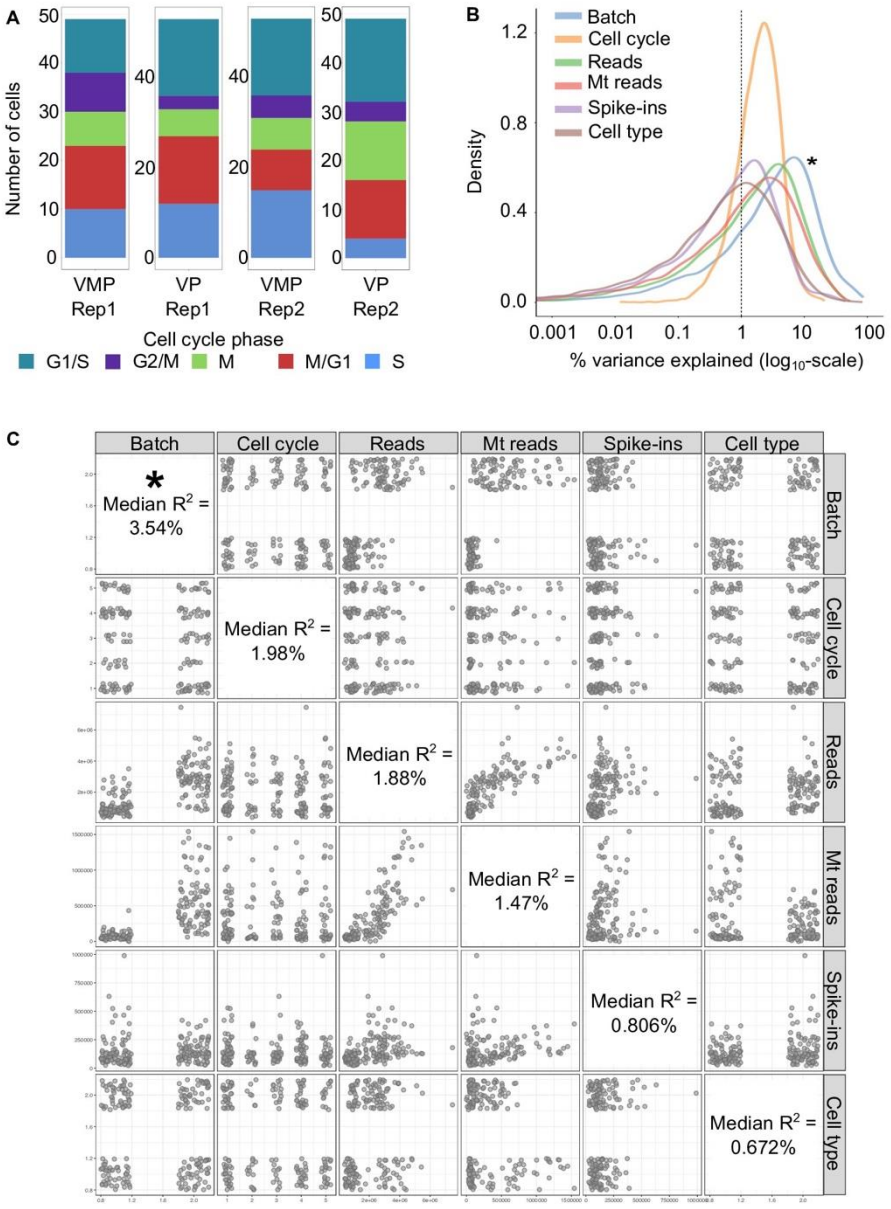

Figure S12 Confounding factors analysis of VMP and VP single cell RNA-sequencing data. **(A)** Stacked bar graph detailing the number of cells in each phase of the cell cycle. A phase-specific score was calculated and cells were assigned to a phase as per (Macosko et al., 2015). **(B)** Density plot of the percentage of variance explained by each technical factor (batch, cell cycle, number of reads, number of mitochondrial reads counts (Mt reads), number of spike-in read counts (Spike-ins) and cell type). Batch effects have the highest percentage of variance explained (*). **(C)** Marginal R^2 for each factor was computed by fitting a linear model regressing read count for each gene against that factor. The median % variance for each factor is shown with only batch effects with a percentage > 3% (*).

Disease Models & Mechanisms • Supplementary information

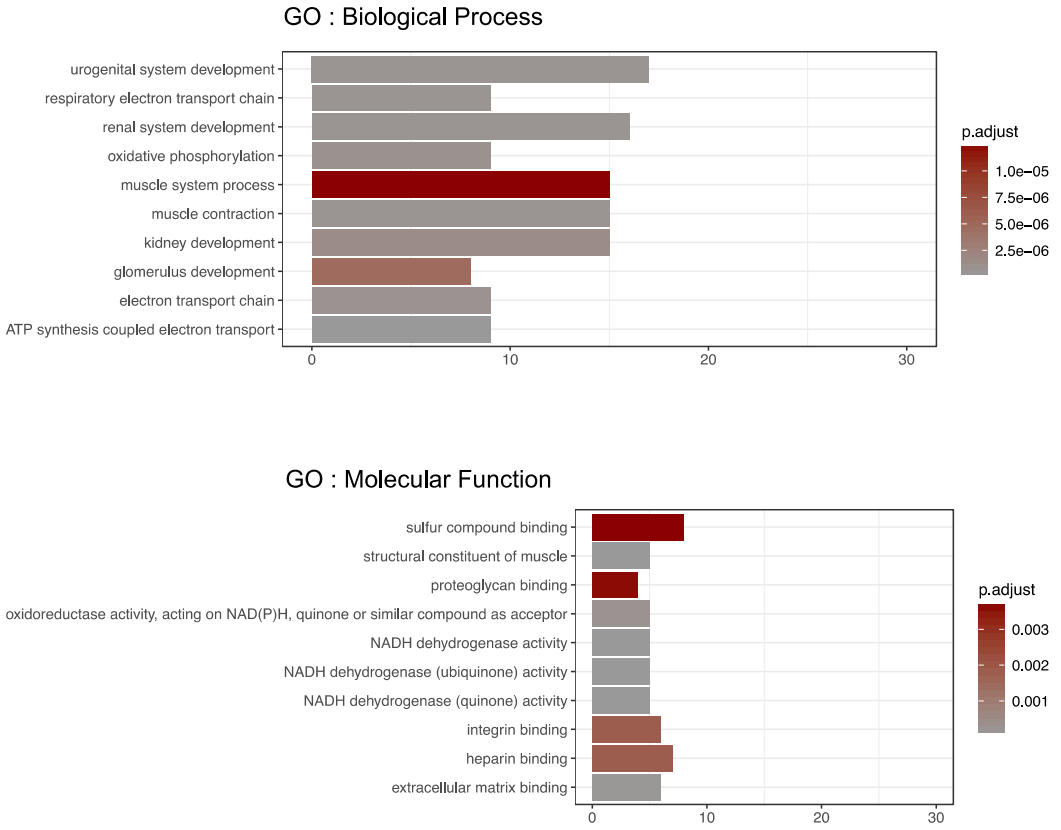

Figure S13 Gene ontology analysis of sexually dimorphic genes derived from single-cell RNA-seq. The figures represent biological process groups and molecular function groups found with an FDR adjusted P-value >0.05 (p-adj.). Bar lengths represent the number of genes in each group and the shade of colour the p-adj for enrichment.

Disease Models & Mechanisms • Supplementary information

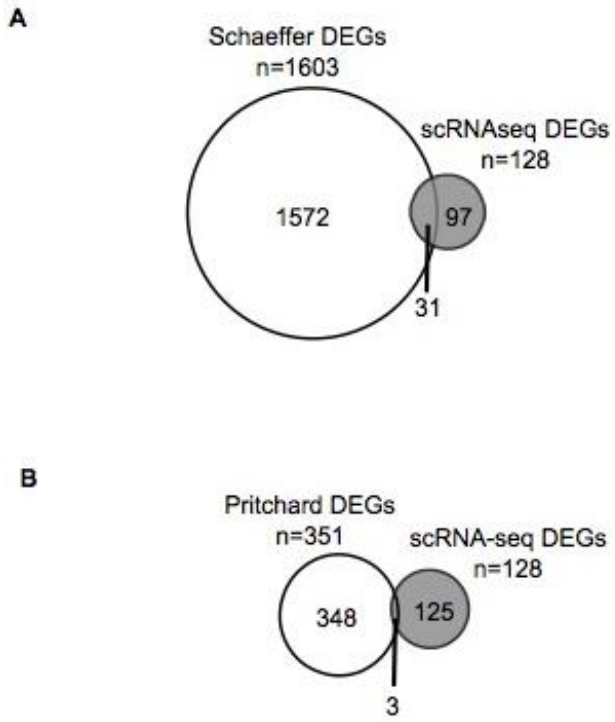

Figure S14 Comparison of sexually dimorphic VMP and VP genes from scRNA-seq with murine androgen-responsive and prostate developmental tissue targets. **(A)** Venn diagrams illustrating the overlap of sexually dimorphic VMP and VP genes derived from single cell RNAseq (scRNA-seq DEGs) with androgen-repsonsive genes from the developing murine urogenital sinus (Schaeffer DEGs) (Schaeffer et al., 2008). **(B)** Venn diagrams illustrating the overlap of sexually dimorphic VMP and VP genes derived from scRNA-seq with markers of murine prostate organogenesis (Pritchard DEGs) (Pritchard et al., 2009).

Disease Models & Mechanisms • Supplementary information

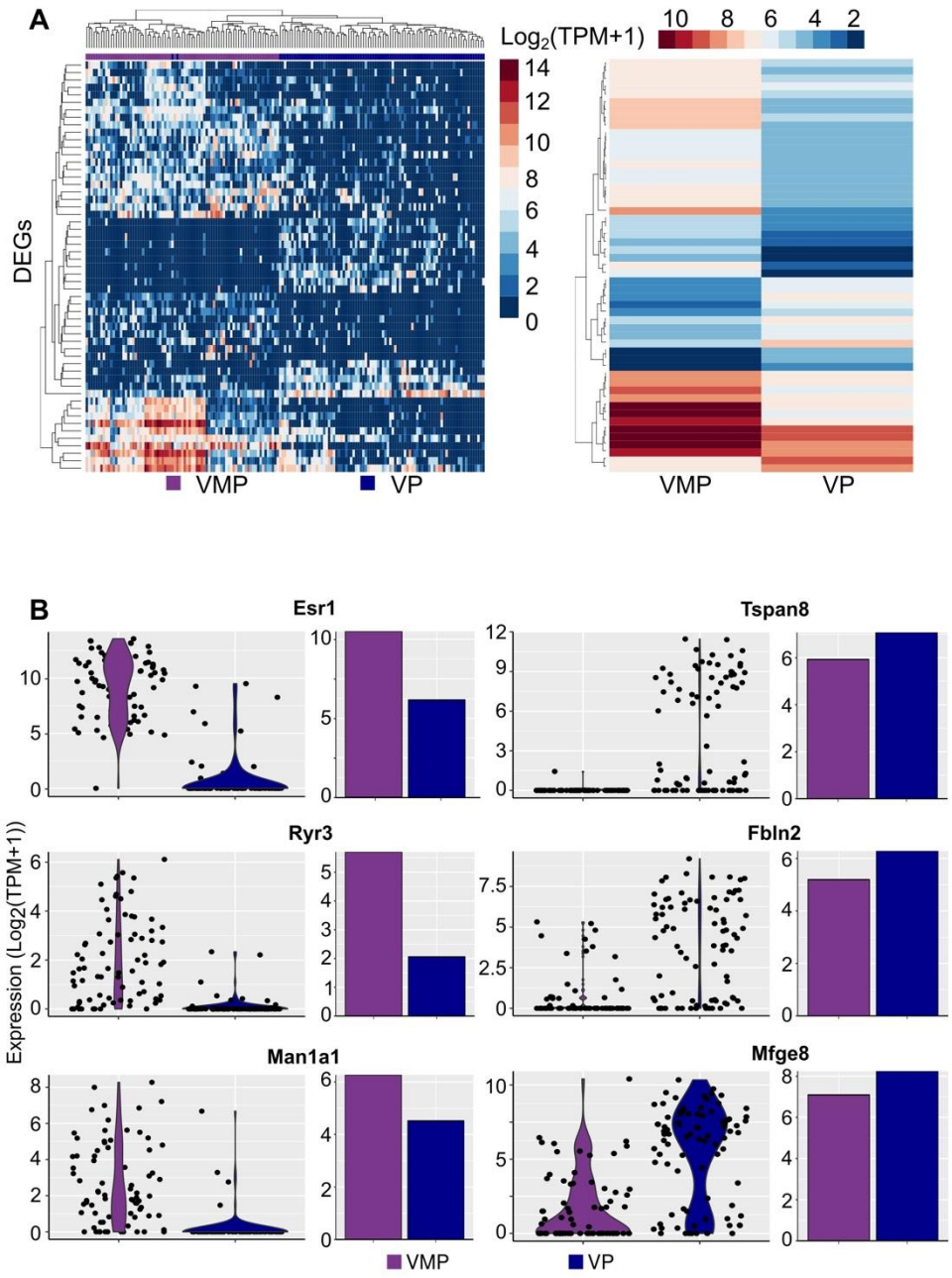

Figure S15 Visualization of tissue and single-cell co-identified differentially expressed genes between VMP and VP. **(A)** Heatmaps representing the $\log_2$ expression values (TPM +1) of the common 53 genes between in VMP and VP single-cells (left) and VMP and VP whole tissues (right). **(B)** Plots showing the distribution of $\log_2$(TPM+1) values across VMP and VP single cells (violin plots) and VMP and VP whole tissues (bar charts) for 3 VMP enriched genes (left column) and 3 VP enriched genes (right column).

Disease Models & Mechanisms • Supplementary information

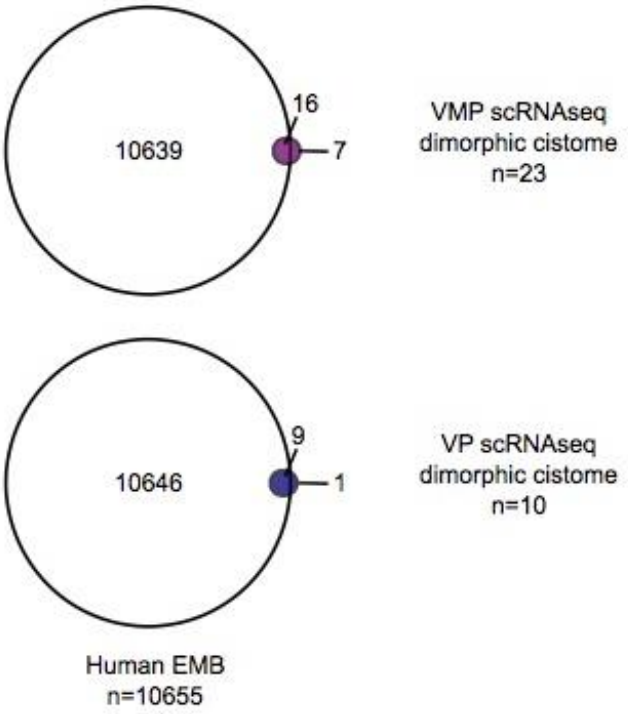

Figure S16 Identification of single cell and tissue RNA-seq co-identified sexually dimorphic VMP and VP AR target genes with human foetal prostate tissue. Venn diagrams illustrating the overlap of sexually dimorphic VMP and VP AR target genes derived from combined single-cell RNAseq and tissue RNAseq with the human foetal prostate transcriptome (Human EMB) (Nash et al., 2018, Orr et al., 2012).

Disease Models & Mechanisms • Supplementary information

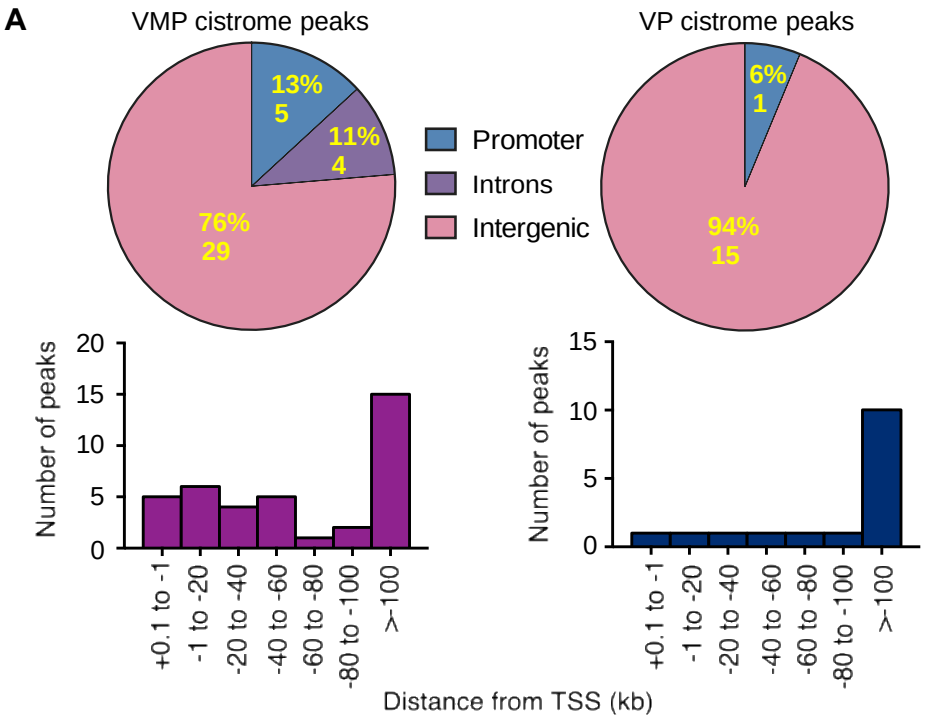

B

	VMP	VP
Top motif		
No. and % peaks with motif	5 (13 %)	3 (19 %)
Best match TF	Stat1	Elf3
TPM (RNAseq)	43.6	56.4

Figure S17 Characterization of AR cistromes between VMP and VP. **(A)** Genomic location analysis of VMP and VP AR cistrome peaks in comparison to the whole genome (rn6). AR cistrome peaks were heavily enriched 76-94% within intergenic regions of the genome with 13% in the promoter regions of genes (-1000bp to +100bp from the transcriptional start site, TSS) in VMP tissues compared with only 6% in VP tissues. The distribution of these peaks upstream from gene TSS are depicted in histograms and show enrichment of AR peaks at distal sites (>100,000kb) from the TSS for both VMP and VP cistrome peaks. **(B)** Motif analysis of the AR DEG cistrome peaks of VMP and VP. Table shows consensus sequence logos of the top sequence motifs identified in VMP and VP using de novo motif analysis with HOMER and an overview of the number of peaks containing the top sequence motif, the best match transcription factor (TF) based on positive mRNA expression from RNA-seq analysis and expression value in transcripts per million (TPM).

Disease Models & Mechanisms • Supplementary information

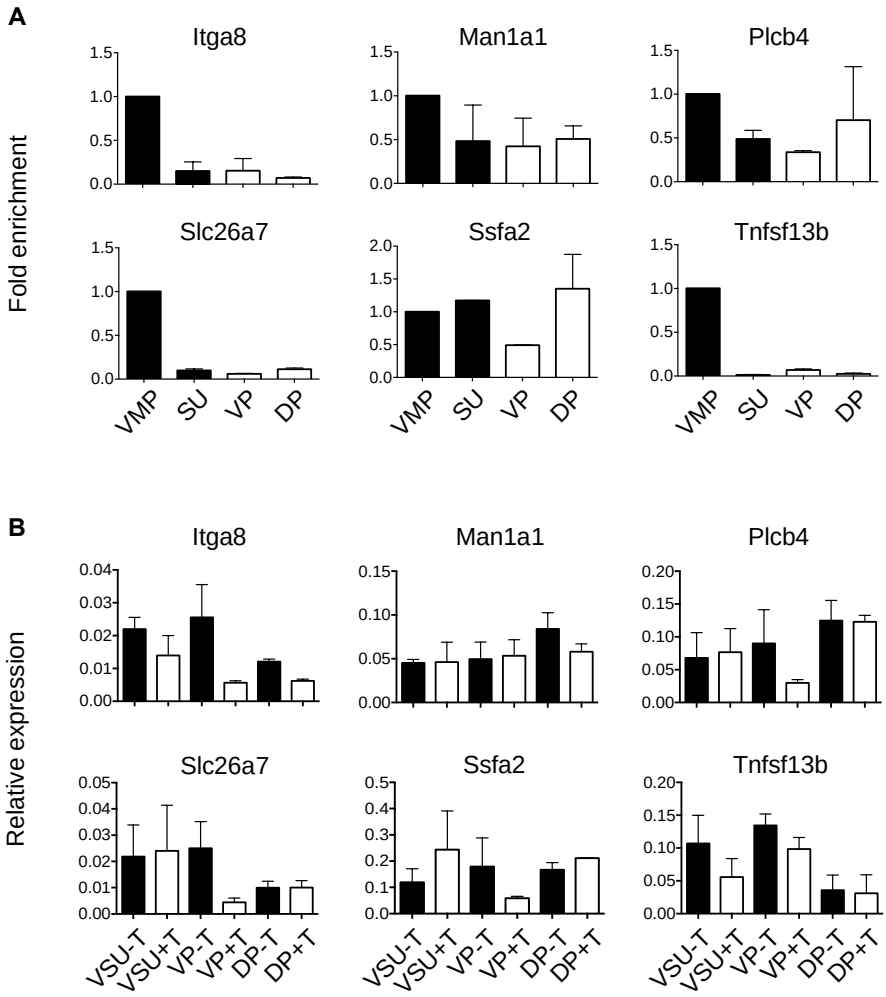

Figure S18 Validation of dimorphism and androgen responsiveness of VMP and VP cistromes in female and male P0 rat whole tissues and ex vivo organ cultures. **(A)** Quantitative real-time PCR (qPCR) of whole VMP, SU, VP and DP tissues. Elevated levels of VMP-enriched cistrome genes were observed vs male tissues. Data is represented as mean fold difference to VMP ± SD of duplicate biological replicate tissue pools (n=2). **(B)** qPCR of ex vivo organ cultures of whole female urogenital tract tissues (containing both VMP and SU, (VSU)), VP and DP tissues treated with 0.01 nM Testosterone (+T) or ethanol (-T) for 24 hours. In most cases, genes are downregulated in response to testosterone in VP and DP organ cultures (all except Man1a1 and Tnfsf13b). Data is represented as relative expression to 4 housekeeping genes ± SD of duplicate biological replicates (n=2).

Disease Models & Mechanisms • Supplementary information

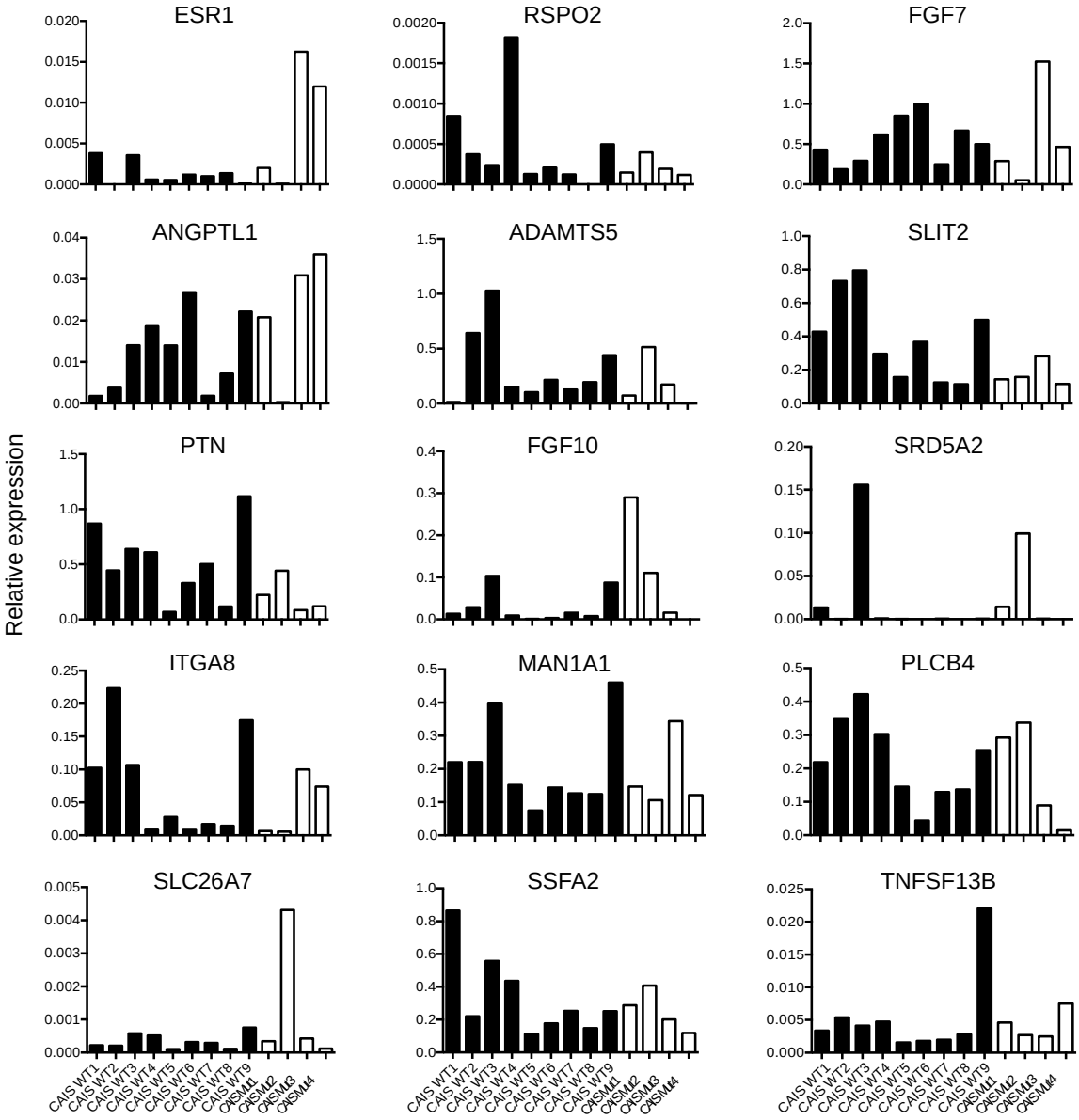

Figure S19 Characterizing expression of VMP and VP cistromes in primary fibroblasts derived from human complete androgen insensitivity syndrome (CAIS) patients. Quantitative real-time PCR (qPCR) of CAIS primary fibroblasts with wild type AR (CAIS WT, black bars) or patients harboring a mutation in AR exons (CAIS Mut, white bars). Variable expression of all cistrome genes were observed across all patients. Data is represented as relative expression to 4 housekeeping genes from one replicate (n=1).

Disease Models & Mechanisms • Supplementary information

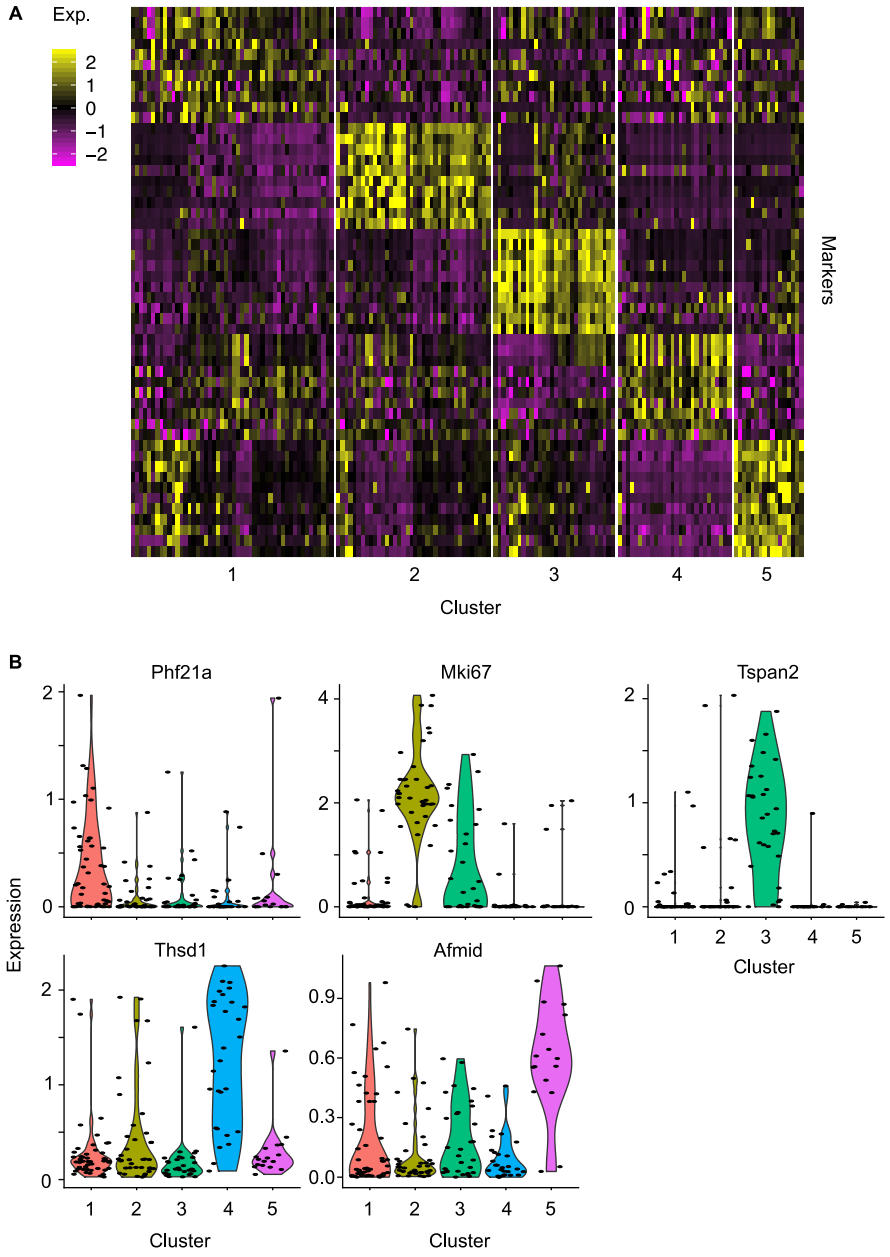

Figure S20 Visualization of discriminatory markers of single-cell clusters. **(A)** Expression heatmap of top 10 discriminatory markers for each VMP and VP cell cluster with a positive expression value and a Bonferroni-Hochberg adjusted p-value <0.05. **(B)** Violin plots showing expression of the top marker of each cluster across VMP and VP cell populations. Width of the violin plot indicates frequency of cells with that expression level. Expression for heatmap and violin plots (Exp.) are presented as normalized, log-transformed and scaled expression relative to all other cells in the dataset.

Disease Models & Mechanisms • Supplementary information

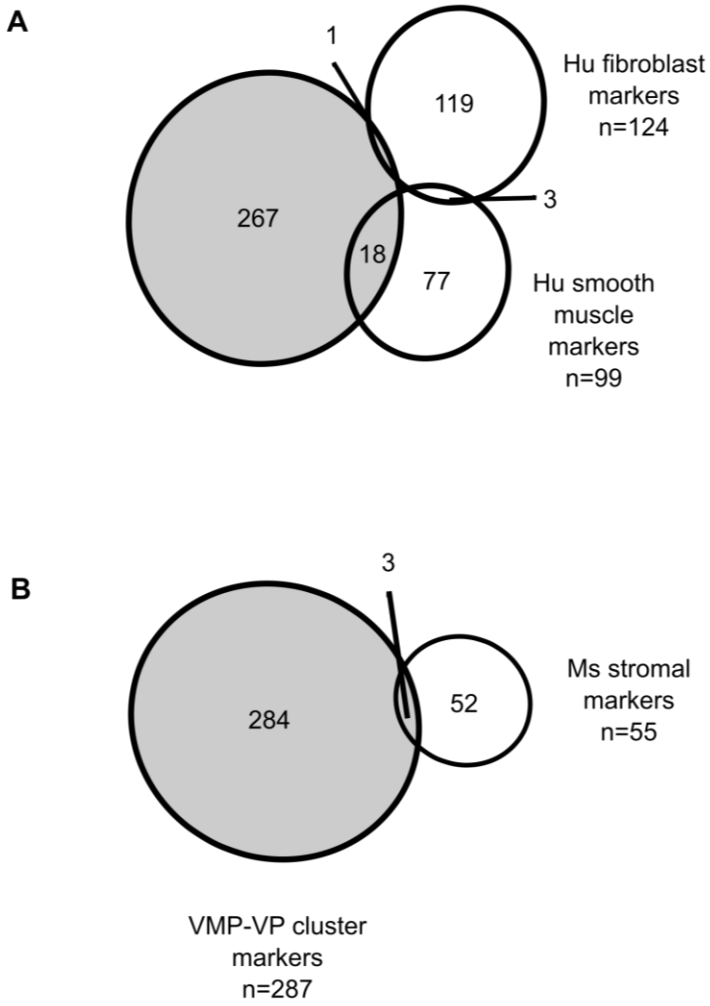

Figure S21 Identification of discriminatory markers of single-cell clusters co-identified with adult prostate cell markers. **(A)** Venn diagrams illustrating the overlap of VMP-VP cluster markers with fibroblast and smooth muscle cell markers from the adult human prostate (Henry et al., 2018). **(B)** Venn diagrams illustrating the overlap of VMP-VP cluster markers with stromal cell markers from the adult mouse prostate (Kwon et al., 2019).

Disease Models & Mechanisms • Supplementary information

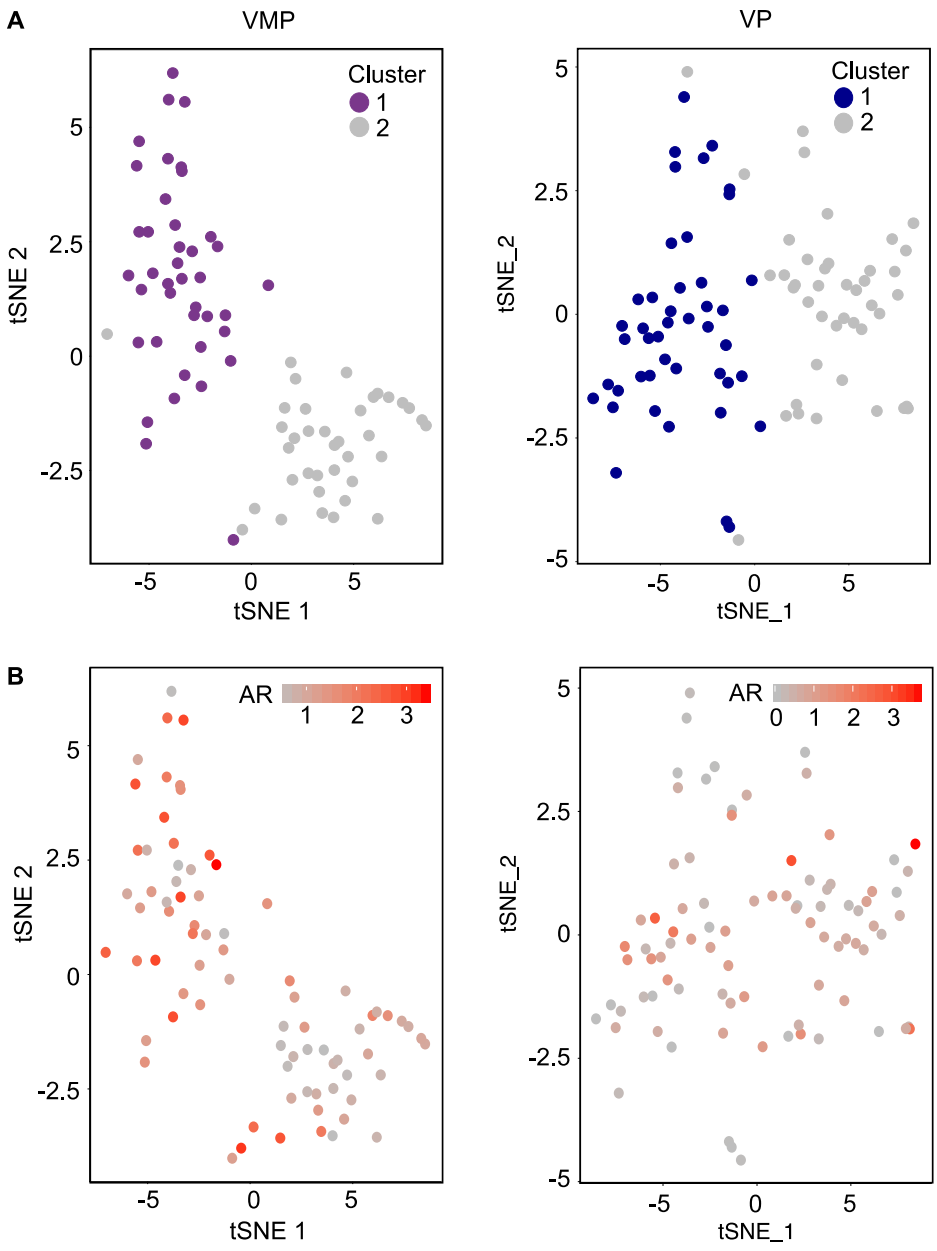

Figure S22 Evaluation of cell heterogeneity within VMP and VP separate datasets and characterization of AR expression across cell subpopulations. **(A)** tSNE analysis identified 2 cell subpopulations VMP and 2 cell subpopulations in VP scRNA-seq separate datasets. **(B)** Visualization of AR expression across VMP and VP cell subpopulations. AR expression is presented as normalized, log-transformed and scaled expression relative to all other cells in the dataset. AR expression shows a random distribution across cells and is not associated with cell subpopulations.

Disease Models & Mechanisms • Supplementary information

Table S1 An overview of mapped reads and called peaks for VMP, SU, VP and DP P0 rat tissues

	VMP	SU	VP	DP	Female Input	Male Input
Total reads	27976217	38240996	33301788	45706554	34718157	41175953
Aligned reads	22424665	30906177	24876770	42655177	28437138	35620000
Filtered reads	16983126	21955725	18180140	18545002	15166441	27138009

Table S2 An overview of average read and gene statistics and cell filtering statistics of single-cell RNA-seq data

Features	VMP Rep1	VP Rep1	VMP Rep2	VP Rep2
Average unique Reads	722491	1498905	2903856	2963736
Average spike-in Reads	93962	200287	157369	147440
Average mitochondrial reads	62444	85194	717199	375672
Average genes	5587	4473	6635	7534
Cells failing mitochondrial QC	2	3	0	2
Cells failing spike-in QC	2	2	1	4
Cells failing library size QC	0	0	4	1
Cells failing gene QC	0	1	1	0
Cells passing QC	46	47	48	44

Data S1. Supplementary tables for Supplementary data

Click here to Download Data S1

Data S2. Supplementary data tables for manuscript figures

Click here to Download Data S2

Disease Models & Mechanisms • Supplementary information

References

HENRY, G. H., MALEWSKA, A., JOSEPH, D. B., MALLADI, V. S., LEE, J., TORREALBA, J., MAUCK, R. J., GAHAN, J. C., RAJ, G. V., ROEHRBORN, C. G., HON, G. C., MACCONMARA, M. P., REESE, J. C., HUTCHINSON, R. C., VEZINA, C. M. & STRAND, D. W. 2018. A Cellular Anatomy of the Normal Adult Human Prostate and Prostatic Urethra. *Cell Rep,* 25**,** 3530-3542.e5.

KWON, O. J., ZHANG, Y., LI, Y., WEI, X., ZHANG, L., CHEN, R., CREIGHTON, C. J. & XIN, L. 2019. Functional Heterogeneity of Mouse Prostate Stromal Cells Revealed by Single-Cell RNA-Seq. *iScience,* 13**,** 328-338.

MACOSKO, E. Z., BASU, A., SATIJA, R., NEMESH, J., SHEKHAR, K., GOLDMAN, M., TIROSH, I., BIALAS, A. R., KAMITAKI, N., MARTERSTECK, E. M., TROMBETTA, J. J., WEITZ, D. A., SANES, J. R., SHALEK, A. K., REGEV, A. & MCCARROLL, S. A. 2015. Highly Parallel Genome-wide Expression Profiling of Individual Cells Using Nanoliter Droplets. *Cell,* 161**,** 1202-1214.

NASH, C., BOUFAIED, N., MILLS, I. G., FRANCO, O. E., HAYWARD, S. W. & THOMSON, A. A. 2018. Genome-wide analysis of AR binding and comparison with transcript expression in primary human fetal prostate fibroblasts and cancer associated fibroblasts. *Mol Cell Endocrinol,* 471**,** 1-14.

ORR, B., RIDDICK, A. C., STEWART, G. D., ANDERSON, R. A., FRANCO, O. E., HAYWARD, S. W. & THOMSON, A. A. 2012. Identification of stromally expressed molecules in the prostate by tag-profiling of cancer-associated fibroblasts, normal fibroblasts and fetal prostate. *Oncogene,* 31**,** 1130-42.

PRITCHARD, C., MECHAM, B., DUMPIT, R., COLEMAN, I., BHATTACHARJEE, M., CHEN, Q., SIKES, R. A. & NELSON, P. S. 2009. Conserved gene expression programs integrate mammalian prostate development and tumorigenesis. *Cancer Res,* 69**,** 1739-47.

SCHAEFFER, E. M., MARCHIONNI, L., HUANG, Z., SIMONS, B., BLACKMAN, A., YU, W., PARMIGIANI, G. & BERMAN, D. M. 2008. Androgen-induced programs for prostate epithelial growth and invasion arise in embryogenesis and are reactivated in cancer. *Oncogene,* 27**,** 7180-91.

Disease Models & Mechanisms • Supplementary information